# Supporting Information to Naus et al. (2018)

## S1 Procedure to obtain hemispheric-average MCF mixing ratios

To aggregate individual measurements of atmospheric air samples to a consistent record of hemispheric average mixing ratios requires correct interpretation of the information contained in the samples. For $CH_4$, $CO_2$ and in principle also for other gases, NOAA has developed a comprehensive interpolation algorithm that approximates these averages. For example, the algorithm functions with gaps in the data and with a changing station network. For MCF, such an algorithm is not available. Instead, we apply an averaging scheme similar to [1]. In this scheme, we first generate monthly means for each station that cover the whole time period of interest. Next, we aggregate the individual stations to hemispheric averages.

Aggregating measurement data to monthly means requires several steps. Firstly, we linearly interpolate between measurements to obtain daily data. These daily averages are then straightforwardly averaged to monthly means. This works reasonably well when each month has one or more measurements available. However, for most stations there are multi-month gaps. If more than one consecutive month is missing, we instead substitute values of nearby stations, corrected by an offset assumed to be constant through time. As an example, the offset between Cape Grim and South Pole is relatively constant, so if either station misses multiple months, a good approximation is obtained by substituting the other's values corrected for by the offset. This works well when multiple stations that represent a similar air mass are available. The exception is the American Samoa Observatory (SMO), for which we only linearly interpolate in time. The implications of this exception are small, as the SMO record has few multi-month gaps in data coverage. Finally, to combine the monthly means of individual stations into hemispheric averages, we compute a weighted average. We combine sites that represent similar air masses in groups. A group's weight reflects the fraction of air mass that the group represents. Mostly, we use the cosine of the average latitude of the sites included in each group. Global mean mixing ratios that were derived using this procedure are shown in Figure S1 (red line in the right panel).

A crucial question in this procedure is how to estimate uncertainties in derived averages. A common technique for estimating uncertainties is a bootstrapping procedure. In bootstrapping, different surface network realizations are randomly generated by counting some stations multiple times, while others are left out entirely. The spread in averages derived from the different network realizations then gives some measure for the uncertainties of these averages. For $CH_4$, this is how the uncertainties reported by NOAA (and used in this study) are derived. For MCF however, fewer stations are available, so that bootstrapping becomes less robust. Moreover, timeseries of annual means per station, as we derive them here, can be interdependent because of the substitution-technique described above. For these reasons, we adopted a different approach to derive uncertainties for MCF.

The procedure we adopt to derive uncertainties for MCF is based on the method presented by [2]. In [2], the annual mean standard deviation (SD) of the MCF timeseries per surface site was used as a measure of the uncertainty in hemispheric means. We also use this measure, but we first remove an exponential trend from the timeseries at each station, before deriving the annual mean SD. This trend removal prevents the long-term trend in the MCF measurements from dominating the derived uncertainties. The SD in the residuals mainly results from source-sink variations, meteorological variability and measurement uncertainty. We deem this a more appropriate measure for uncertainty than the long-term trend. The trend removal reduces the annual mean SD per station from around 5% (as in [2]) to 1.5%. Next, we use a Monte-Carlo simulation to propagate the uncertainty per station to an uncertainty in the global and hemispheric means. In the Monte-Carlo simulation, we perturb the annual means per station proportional to the annual mean SD per station, and derive new global and hemispheric means. The SD of each quantity derived from the resulting ensemble is used as a measure for uncertainty. This Monte-Carlo approach accounts for the fact that stations are not expected to be influenced by the same variability at the same time, so that their errors should be largely uncorrelated. The time-dependent uncertainties in the global mean growth rate and in the rate of change of the IH gradient vary between 0.5−0.7% and 1.0−1.5% respectively. As can be expected from the

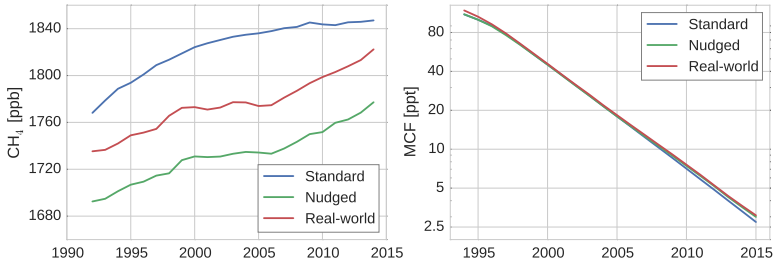


**Figure S1:** Global, annual mean mixing ratios for $CH_4$ (left) and MCF (right) as derived from model-sampled observations from the standard and nudged simulation, and from real-world NOAA observations.

modifications we have made to their method, this is significantly lower than the uncertainties adopted by [2], though still higher than the errors derived from the TM5 simulations (see Table 2).

The timeseries of MCF we have derived, along with the corresponding uncertainties, are presented in a supplemental dataset, along with the same parameters for $CH_4$.

# S2 The nudged simulation

In this supplement, we discuss the nudged simulation and some of its results. In the nudged simulation, we nudged the model to observations from NOAA surface sites, following a procedure analogous to [3]. In essence the nudging approach is a crude mass-balance inversion. We compared modelled mixing ratios at ground level at the dateline to latitudinally interpolated, monthly mean observations from the NOAA network, under the assumption that both of these are representative of the background atmosphere at that latitude. Then, we scaled the entire latitude band according to the model-to-observation ratio using a relaxation time of 100 days, to ensure that the model follows the long-term trend in real-world observations. Since the nudging does not depend on the a priori emission and loss fields, the nudged run provides a good test for the sensitivity of our conclusions to the source-sink distribution used.

Figure S1 shows the global, annual mean mixing ratios of MCF and $CH_4$ as derived from model-sampled observations in the standard simulation and in the nudged simulation, and as derived from real-world NOAA data. For all three timeseries, the same averaging algorithms are used. The standard simulation for $CH_4$ performs poorly, as can be expected from a simulation with annually repeating emissions and constant loss fields. The nudged run captures the rough characteristics of $CH_4$ growth rate variations much better: the 2000-2006 stagnation and the renewed growth after 2007 are reproduced quite well. For MCF, the standard run already captured the important aspects of the global atmospheric decline. However, from 2008 onwards the standard simulation increasingly underestimated MCF mixing ratios. Therefore, the nudged run tends to add MCF towards the end of the simulation.

Observations sampled from the nudged run and real-world NOAA observations still differ for two reasons. Firstly, for the nudging, we do not compare mixing ratios at the site location, but at the dateline. Because we scale the entire latitude band in the lower atmosphere, also the site location is nudged, but only indirectly. This difference is likely driving the systematic offset between annual means derived from the nudged runs and from the real-world annual means of $CH_4$ (left panel in Figure S1). At the dateline itself, the latitudinal fields used for nudging and the its modelled counterpart overlap near perfectly. Secondly, only a subset of the measurement sites that are used for averaging are used for nudging. We want to stress that the resulting differences are not important for our purposes, as our main objective was to test the sensitivity to a different, somewhat more realistic emission distribution, rather than a provide a full inversion.

To give an impression of the nudging strength, Figure S2 shows the global emissions both from the standard and from the nudged TM5 simulation, if the derived nudging term (positive or negative) is assumed indicative of variations in emissions. Note that this interpretation is arbitrary, as nudging can also indicate

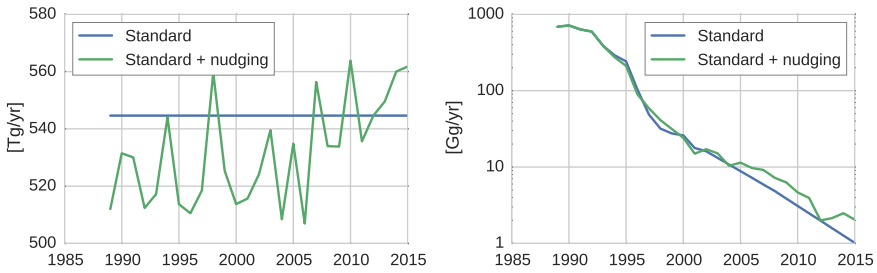


**Figure S2:** Global, annual emissions of $CH_4$ (left) and MCF (right). Standard emissions are the emissions as used in all our TM5 simulations, while the standard+nudged emissions are the result of adding the global, annual mean nudging to the standard emissions.

variations in the loss fields. For $CH_4$, nudging can be quite extreme, with interannual variations of up to 40 Tg/yr. Though part of these emission variations may be real, the extreme extent of the variations likely results from overfitting or incorrect assignment of emissions to certain latitudes. This reveals the limitations of the nudging approach. For MCF, there is a clear need for additional emissions in later years with respect to our initial assumption that emissions decline with 20%/year after 2006. Since differences in MCF mixing ratios between the standard run and real-world observations were especially high at Mace Head (not shown), this would indicate some ongoing European emissions.

# S3 Interhemispheric asymmetries in correlations between k, OH and $CH_4$/MCF

## S3.1 Introduction

In Section 3.1.3 it is outlined that the IH OH ratio to be used in a two-box model is not necessarily the same as the physical IH OH ratio. For example, in our 3D simulations runs, the IH ratio of the OH fields is 0.98, while the OH ratio seen by $CH_4$ is 1.05: a difference of 7%. The differences are a result of first averaging k, OH, and $CH_4$/MCF per hemisphere, per year individually, and subsequently calculating the hemispheric loss (as in a box model), compared to a 3D model, where the loss is integrated over the cells that make up the hemisphere. Because of spatio-temporal correlations between the parameters involved (OH, $k_{OH}$, tracer distribution) and from hemispheric asymmetries in these correlations, differences between these two approaches arise. In this section, we outline in more detail which correlations predominantly drive the differences.

First, we define the ratio $r$ in equation 1. The overline denotes the average over spatial and/or temporal dimensions. The ratio $r$ is unity for uncorrelated parameters, and $r > 1$ for positive and $r < 1$ for negative correlations. The ratio $rr$ denotes the IH ratio of $r$ (Equation 2). If $rr > 1$, the correlation is stronger in the NH than in the SH, and the reverse is the case for $rr < 1$. Thus, while $r$ is a measure for the strength of the correlation in one hemisphere, $rr$ is a measure for the IH asymmetry in this correlation.

$$r[a, b, ...] = \frac{\overline{a\ b\ ...}}{\overline{a}\ \overline{b}\ ...} \tag{1}$$

$$rr[a, b, ...] = \frac{r[a, b, ...]_{NH}}{r[a, b, ...]_{SH}} \tag{2}$$

Ratios $rr[k, OH, CH_4]$ and $rr[k, OH, MCF]$ were both found to deviate significantly from 1 in the 3D simulations we used to tune our two-box model. This means that multiplying the hemispheric, annual

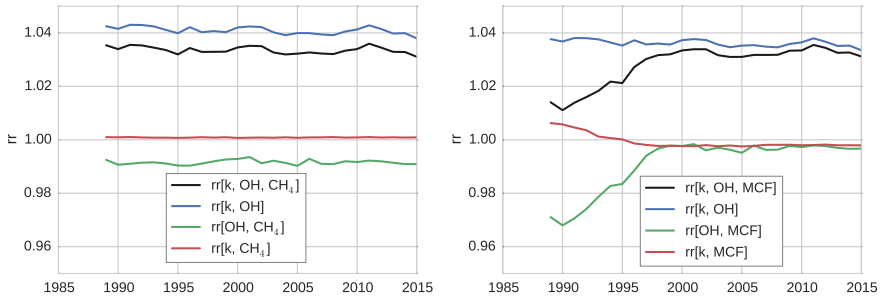


**Figure S3:** The annually averaged $rr$ ratios, as defined in Equation 2, for the different components of chemical loss of $CH_4$ (left) and MCF (right).

averages of each parameter in a two-box model does not reproduce the loss rate calculated in the full 3D simulation. We emphasize that this result and the following analysis are specific to the OH field described in [4] and the implementation in TM5. There are three correlations that can drive the difference: between $k_{OH}$ and OH, between $k_{OH}$ and $CH_4$/MCF and between OH and $CH_4$/MCF. The contributions by each of these three to the asymmetry is shown in Figure S3. From this figure, it can be inferred that the main driver of both $rr[k_{OH}, OH, CH_4]$ and $rr[k_{OH}, OH, MCF]$ being greater than 1 is the correlation between $k_{OH}$ and OH, while the time-dependent behaviour of the IH OH ratio of MCF is driven predominantly by the correlation between OH and MCF. In the following, we discuss each of the three correlations in more detail.

## S3.2 Correlation between reaction coefficient $k_{OH}$ and OH

As the reaction coefficient $k_{OH}$ of both MCF and $CH_4$ are a direct function of only temperature (T), the spatial distribution of $k_{OH}$ and T are identical. For this reason, the correlation between $k_{OH+CH_4}$ and OH and $k_{OH+MCF}$ and OH are similar. Here, we discuss only $k_{OH+CH_4}$. OH and $k_{OH}$ are strongly positively correlated: spatially, with maxima in the tropics, and minima at the poles; and temporally, with maxima in the summer hemisphere and minima in the winter hemisphere. However, this correlation is stronger in the NH than in the SH, resulting in $rr[k_{OH}, OH] > 1$ (blue lines in Figure S3; black line in Figure S4). This effect turns out to be the main driver of both $rr[k_{OH}, OH, CH_4]$ and $rr[k_{OH}, OH, MCF]$ being greater than 1. The asymmetry is the integrated effect of correlations in the latitudinal, longitudinal, vertical and seasonal dimension. To assess the contribution of each dimension to the correlation asymmetry, we first averaged $k_{OH+CH_4}$ and OH over all but one dimension before computing $rr$. In this way, we isolate the influence of one dimension on the asymmetry. The result is shown in Figure S4.

The largest effect is seen when isolating the vertical dimension, which gives an $rr$ close to the full $rr$ (red line in Figure S4). Further analysis reveals that this is because the vertical distribution of OH in the NH and SH is different. More precisely, the maximum in OH is located at lower altitude in the NH than in the SH (Figure S5). This is likely driven by higher $NO_x$ emissions in the NH, which increases OH recycling close to the surface ( [4]). At lower altitudes temperatures are higher, and as a consequence the correlation between $k_{OH}$ and OH is strongest in the NH.

An effect in the same direction is seen for the seasonal component. Figure S6 shows the seasonal cycle of OH and $k_{OH+CH_4}$ in each hemisphere. In the NH, the two seasonal cycles are very well in line, while in the SH less so. Moreover, the seasonal cycle in temperature in the NH is stronger than in the SH. Both effects are likely a consequence of the higher land fraction in the NH, which results in a lower surface heat capacity. This drives a stronger and more direct response of temperature to seasonal variations in solar irradiance.

Finally, there is an opposing asymmetry in the latitudinal correlation. Figure S7 shows that tropical OH is highest in the SH, whereas extra-tropical OH is highest in the NH. As temperatures are highest in the tropics, the correlation between temperature and OH is highest in the SH.

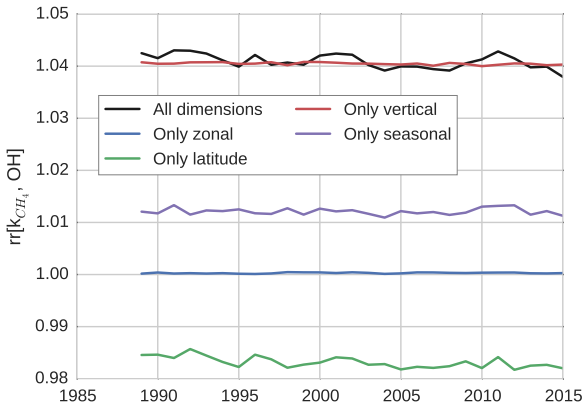


**Figure S4:** The annually averaged evolution of the $rr[k_{CH_4}, OH]$ ratio, as defined in Equation 2. The contribution from each dimension is isolated by only considering that dimension for the $rr$ ratio. Note that the black line corresponds to the blue line in the left panel of Figure S3

As expected, the dimension of longitude has only a small effect: both temperature and OH are relatively uniform zonally (not shown).

### S3.3 Correlation between OH and $CH_4$/MCF

Figure S3 shows that the trend in the IH OH ratio of MCF is largely driven by the $rr[OH, MCF]$ component of the correlation. It follows intuition that when the distribution of MCF strongly changes, then also the MCF distribution with respect to OH changes. Similar to $rr[k, OH]$, we can isolate the influence of each dimension on the asymmetry in the correlation (Figure S8).

The largest contribution to $rr[OH, MCF]$ comes from the latitudinal component (green line in Figure S8). This is driven by the decreasing IH MCF gradient through time (Figure S9). Initially, MCF decreases towards the tropics in the NH, and increases towards the tropics in the SH. As OH is highest in the tropics, MCF and OH are negatively correlated in the NH and positively correlated in the SH. This drives $rr[OH, MCF] < 1$. The IH gradient largely disappears over time, so that $rr[OH, MCF]$ approaches 1.

A weaker, opposite effect is seen in the vertical. Initially, NH MCF decreases with altitude strongly, while SH MCF slightly increases with altitude (Figure S10). As OH maximizes at low altitude, this drives a positive correlation in the NH, compared to the weak negative correlation in the SH. This results in an $rr[OH, MCF] > 1$. As the gradients disappear over time, so too does the asymmetric correlation.

For $CH_4$, spatio-temporal gradients are smaller. However, it too has an $rr[OH, CH_4] < 1$, mostly due to the IH gradient in $CH_4$.

### S3.4 Correlation between reaction coefficient $k_{OH}$ and $CH_4$/MCF

As indicated earlier, correlations between $k$ and OH are very high, and thus the correlation between $k_{OH}$ and $CH_4$/MCF behaves largely similar to the correlation between OH and $CH_4$/MCF. However, interestingly, the net effect on $rr$ can be opposite. In the early 90s, we find a positive trend in $rr[OH, MCF]$, while the trend in $rr[k_{OH+MCF}, MCF]$ is negative (right panel in Figure S3). This is because temperature, and thus $k$, have stronger and more unidirectional gradients in the vertical, compared to OH. Therefore, the correlation between mixing ratios and $k$ is dominated by the vertical dimension, whereas the correlation between OH and mixing ratios is dominated by the latitudinal dimension. This detail reveals the intricacies of the compensating effects in the final $rr$ ratio, and thus of the resulting IH OH ratio seen by different tracers.

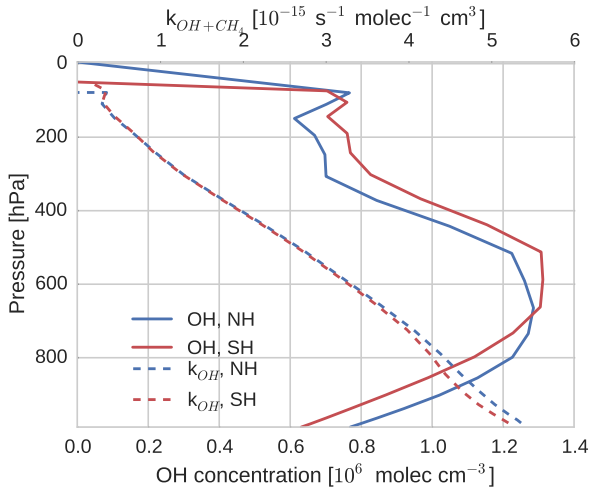


**Figure S5:** The average vertical distribution of tropospheric OH (solid lines, bottom y-axis) and $k_{OH+CH_4}$ (dashed lines, top y-axis) NH (blue) and in the SH (red).

### S3.5 Conclusion

In conclusion, the symmetry between the NH and the SH that is implicitly assumed in the typical two-box set-up does not necessarily hold. This means that different tracers potentially require different IH OH ratios. That different tracers might be exposed to different atmospheric oxidative capacities has been noted before [5]. However, we quantify exactly the contributions of different parameters and dimensions on the ratio. The most important implication of this analysis is the sheer number of parameters that the final OH ratio hinges on (e.g. IH gradient; vertical profile; temperature dependence of $k_{OH}$). This makes it very difficult to predict how the ratio would vary under changing conditions and for different tracers. Of course, our results depend strongly on the specific OH distribution and 3D transport model that is used, but the OH distribution and 3D model we use has been shown to result in realistic $CH_4$ mixing ratio fields ( [6]; [7]). Moreover, the observation that such large deviations between tracers and in time are possible, will likely hold for any OH distribution and 3D transport model.

## References

[1] S. A. Montzka, M. Krol, E. J. Dlugokencky, B. Hall, P. Jöckel, and J. Lelieveld. Small interannual variability of global atmospheric hydroxyl. *Science*, 331(6013):67–69, 2011.

[2] M. Rigby, S. A. Montzka, R. G. Prinn, J. W. C. White, D. Young, S. ODoherty, M. F. Lunt, A. L. Ganesan, A. J. Manning, P. G. Simmonds, et al. Role of atmospheric oxidation in recent methane growth. *Proceedings of the National Academy of Sciences*, 114(21):5373–5377, 2017.

[3] N. Bândă, M. Krol, T. Noije, M. Weele, J. E. Williams, P. Le Sager, U. Niemeier, L. Thomason, and T. Röckmann. The effect of stratospheric sulfur from Mount Pinatubo on tropospheric oxidizing capacity and methane. *Journal of Geophysical Research: Atmospheres*, 120(3):1202–1220, 2015.

[4] C. M. Spivakovsky, J. A. Logan, S. A. Montzka, Y. J. Balkanski, M. Foreman-Fowler, D. B. A. Jones, L. W. Horowitz, A. C. Fusco, C. A. M. Brenninkmeijer, M. J. Prather, et al. Three-dimensional climatological distribution of tropospheric OH: Update and evaluation. *Journal of Geophysical Research: Atmospheres*, 105(D7):8931–8980, 2000.

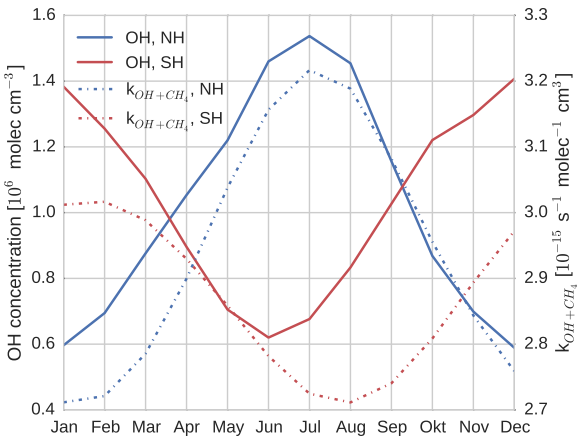


**Figure S6:** The seasonal cycle of tropospheric OH (left axis, solid lines) and $k_{OH}$ (right axis, dashed lines) in the NH (blue) and in the SH (red).


[5] M. G. Lawrence, P. Jöckel, and R. von Kuhlmann. What does the global mean OH concentration tell us? *Atmospheric Chemistry and Physics*, 1(1):37–49, 2001.

[6] P. K. Patra, S. Houweling, M. C. Krol, P. Bousquet, D. Belikov, D. Bergmann, H. Bian, P. Cameron-Smith, M. P. Chipperfield, K. Corbin, et al. TransCom model simulations of $CH_4$ and related species: linking transport, surface flux and chemical loss with $CH_4$ variability in the troposphere and lower stratosphere. *Atmospheric Chemistry and Physics*, 11(24):12813–12837, 2011.

[7] V. Huijnen, J. Williams, M. van Weele, T. van Noije, M. C. Krol, F. Dentener, A. Segers, S. Houweling, W. Peters, J. de Laat, et al. The global chemistry transport model TM5: description and evaluation of the tropospheric chemistry version 3.0. *Geoscientific Model Development*, 3(2):445–473, 2010.

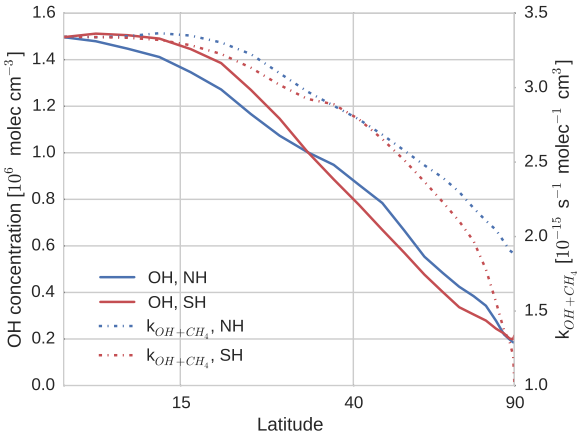


**Figure S7:** The latitudinal distribution of tropospheric OH (left axis, solid lines) and $k_{OH}$ (right axis, dashed lines) in the NH (blue) and in the SH (red).

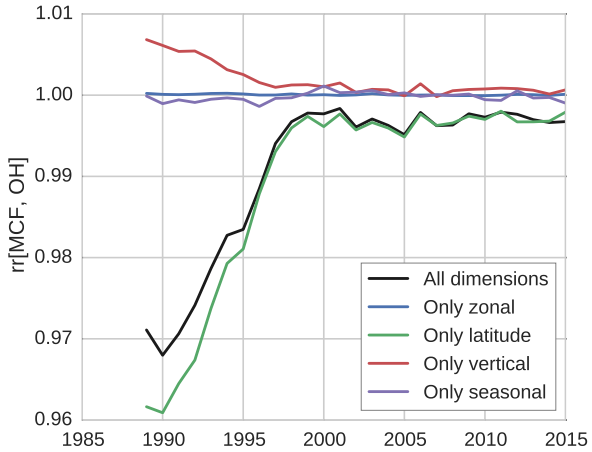


**Figure S8:** The annually averaged evolution of the $rr[MCF, OH]$ ratio, as defined in Equation 2. The contribution from each dimension is isolated by only considering that dimension for the $rr$ ratio. Note that the black line corresponds to the green line in the right panel of Figure S3

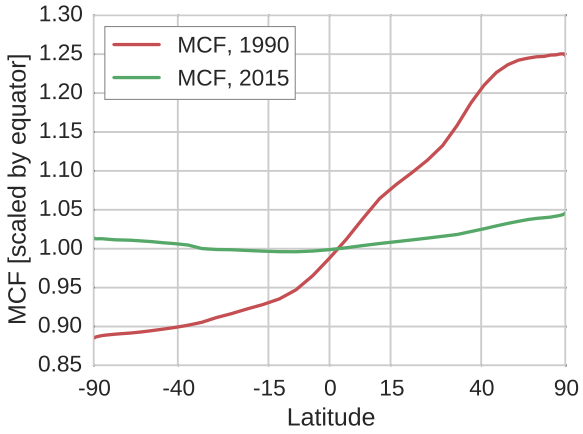


**Figure S9:** The latitudinal distribution of MCF in 1990 and in 2015. MCF mixing ratios are scaled by MCF mixing ratios at the equator.

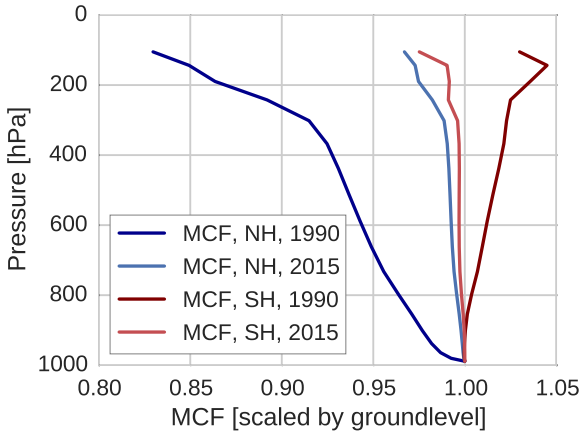


**Figure S10:** The vertical distribution of MCF in 1990 and in 2015. MCF mixing ratios are scaled by ground-level MCF.